

Electron-Conducting PbS Nanocrystal Superlattices with Long-Range Order Enabled by Terthiophene Molecular Linkers

Alexander André,[†] Michelle Weber,[†] Kai M. Wurst,[†] Santanu Maiti,^{‡,§} Frank Schreiber,^{‡,§} and Marcus Scheele^{*,†,§}

[†]Institute for Physical and Theoretical Chemistry, University of Tübingen, Auf der Morgenstelle 18, 72076 Tübingen, Germany

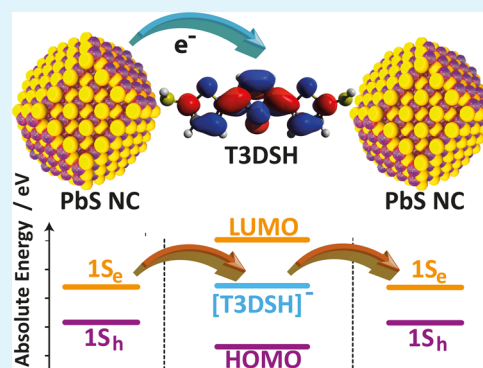
[‡]Institute of Applied Physics, University of Tübingen, Auf der Morgenstelle 10, 72076 Tübingen, Germany

[§]Center for Light-Matter Interaction, Sensors & Analytics LISA⁺, University of Tübingen, Auf der Morgenstelle 15, 72076 Tübingen, Germany

Supporting Information

ABSTRACT: PbS nanocrystals are surface-functionalized with the organic semiconductor 5,5''-dithiol-[2,2':5,2''-terthiophene] and assembled to afford hybrid nanostructured thin films with a large structural coherence and an electron mobility of 0.2 cm²/(V s). Electrochemistry, optical spectroscopy, and quantum mechanical calculations are applied to elucidate the electronic structure at the inorganic/organic interface, and it is established that electron injection into the molecule alters its (electronic) structure, which greatly facilitates coupling of the neighboring PbS 1S_e states. This is verified by field-effect and electrochemically gated transport measurements, and evidence is provided that carrier transport occurs predominantly via the 1S_e states. The presented material allows studying structure–transport correlations and exploring transport anisotropies in semiconductor nanocrystal superlattices.

KEYWORDS: semiconductor nanocrystals, organic π -systems, electrochemical gating, spectroelectrochemistry, electric transport, X-ray scattering



INTRODUCTION

Coupled organic–inorganic nanostructures (COINs) exploit the electronic interactions between an inorganic nanocrystal (NC) core and its organic ligand shell.^{1–4} By replacing the insulating surface molecules typically introduced during synthesis with molecules of tailored functionalities, new functional, e.g., optical and electronic, properties can be obtained. As a result, enhanced photovoltaic conversion efficiencies, increased catalytic activity, facilitated energy transfer, and photon upconversion have been realized.^{5–9} Specifically, COINs based on lead chalcogenide NCs are widely applied in optoelectronics due to a large size tunability of the band gap and high intrinsic charge carrier mobilities.^{10–12} In the case of solar cells for example, high carrier mobilities reduce the exciton recombination probability and, thus, can enhance the overall efficiency.^{5,13} Optimizing carrier mobilities in lead chalcogenide NCs has been especially difficult for electron transport, and a number of different protocols have been implemented to overcome this obstacle.^{14–20} Our strategy in this respect is to use fully conjugated, bidentate molecules with strongly binding functional groups as surface ligands.^{21,22} These ligands act as electronic linkers to improve the interparticle charge carrier transport by providing matching energy levels for the NC 1S_h and 1S_e states.^{3,23} A serious challenge is that long and conjugated molecules maintain structural order and orientation

in the NC ensemble, which are often lost during ligand exchange with short molecules.^{24,25} Due to the low electrochemical potential of the 1S_e state of lead chalcogenide NCs (–3.5 to –4 eV vs vacuum), identifying conjugated molecules suitable for promoting electron transport in these materials is a challenge that remains to be addressed.^{26–28}

Here, we report PbS NC solids cross-linked with the bidentate organic semiconductor 5,5''-dithiol-[2,2':5,2''-terthiophene] (T3DSH). Although charge transfer between NCs and oligothiophenes has been studied previously, functional electronic devices with an efficient electron transport have not been reported.^{29–34} We demonstrate field-effect transistor (FET) electron mobilities of 0.2 cm²/(V s) as well as macroscopic structural coherence in superlattices of T3DSH-functionalized PbS NCs. With a combination of cyclovoltammetry (CV), spectroelectrochemistry, electrochemically gated (EG) conductivity measurements, and quantum chemical calculations, we reveal the pivotal role of the electronic structure of T3DSH in aiding electron transport through the PbS NC superlattice.

Received: April 14, 2018

Accepted: July 3, 2018

Published: July 3, 2018

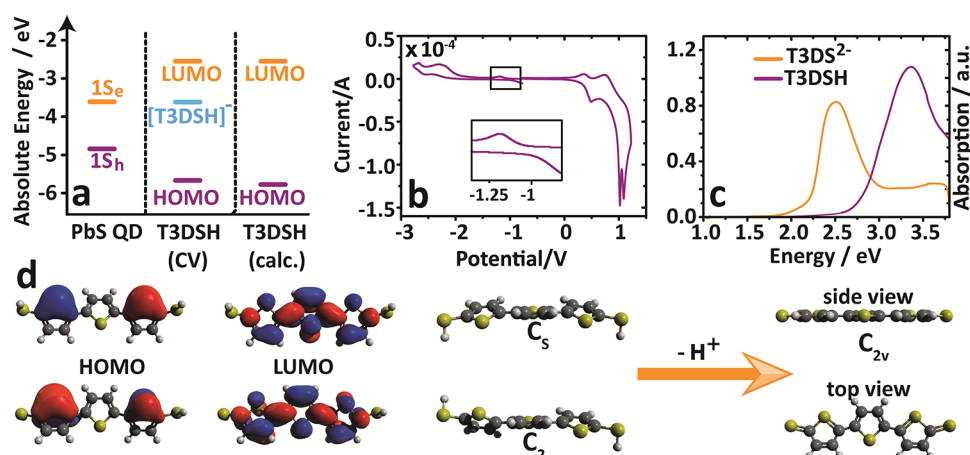


Figure 1. (a) Relevant energy levels for PbS NCs, according to previous density functional theory (DFT) calculations,²¹ and for T3DSH as calculated from CV and DFT. The state labeled “[T3DSH]⁻” corresponds to the signal magnified in the CV measurement and is attributed to charging of the parent T3DSH compound. (b) CV measurement of T3DSH dissolved in acetone referenced vs Fc/Fc⁺. (c) UV–vis measurement of T3DSH and its deprotonated derivate T3DS²⁻ in acetone. (d) Calculated frontier orbitals and molecular geometry of the two isoenergetic conformers of T3DSH with C_s and C₂ symmetry, respectively, as well as the structural change after deprotonation to T3DS²⁻ with C_{2v} symmetry.

Table 1. HOMO and LUMO Energies of T3DSH as Calculated with Different Methods and Basis Sets^a

method	B3LYP		B3LYP/PCM	CCSD	CCSD/PCM	exp.
	6-311+G**	aug-TZvP	6-311+G**	6-311+G**	6-311+G**	CV
HOMO	7.46 ± 0.01	7.42 ± 0.01	5.92 ± 0.01	7.45 ± 0.01	5.92 ± 0.01	5.7 ± 0.1
LUMO	0.71 ± 0.01		2.49 ± 0.01			

^aMolecule solvation is modeled using the PCM method. Ground-state geometries are calculated using B3LYP or B3LYP with PCM, respectively. The values are compared with the experimental value from CV measurements. All energies are in electronvolts and have been referenced against the vacuum level.

RESULTS AND DISCUSSION

We use CV, optical spectroscopy, and quantum chemical calculations to arrive at the electronic structure at the interface between PbS NCs and T3DSH schematically depicted in Figure 1a. The position of the first excited hole (1S_h) and electron state (1S_e) of the PbS NCs are inferred from previous experimental and theoretical studies of this material, including polarization effects.^{21,26–28} The energies of the highest occupied and the lowest unoccupied molecular orbitals (HOMO and LUMO, respectively) of T3DSH are determined by CV in a 0.1 M solution of tetrabutylammonium hexafluorophosphate (TBAHFP) in acetone at a scan rate of 0.1 V/s (Figure 1b). The potential is referenced against the ferrocene/ferrocenium (Fc/Fc⁺) couple, assumed to be at 4.8 eV below vacuum.³⁵ In accordance with Bao and co-workers, we find a split oxidation wave at 0.9 V vs Fc/Fc⁺ (−5.7 eV below vacuum) and attribute it to charging of the molecule’s HOMO level.³⁶ We note a weaker oxidation wave at 0.4 V and tentatively attribute this process to dimerization, which is often observed for oligothiophenes around this electrochemical potential.^{37,38} In the CV’s reductive path, we observe a strong reduction peak at −2.3 V and a weaker signal at −1.2 V vs Fc/Fc⁺. In line with an optical HOMO–LUMO gap of approximately 3 eV (λ_{max} = 378 nm) for T3DSH in acetone (Figure 1c), we assign the reduction wave at −2.3 V (−2.5 eV below vacuum) to the charging of the LUMO for an electrochemical HOMO–LUMO gap of 3.2 eV.

To support the CV data, we perform quantum chemical calculations by applying methods based on the extensive work on thiophenes by Kölle et al.³⁹ The geometry of T3DSH is optimized utilizing the B3LYP functional and the 6-311+G**

basis set. Two energetically very close conformations exist for the minimum geometry of T3DSH: the trans-, trans-, trans-geometry with C₂ symmetry and the trans-, trans-, cis-geometry with C_s symmetry.³⁹ Single-point calculations were performed with the CCSD and the DFT level of theory, using the 6-311+G** basis set. As the standard calculation of a molecule in vacuum poorly reflects the scenario of an either solvated or otherwise bound molecule, we corrected for solvation effects via the polarizable continuum model (PCM) and acetone as the solvent.^{40,41} The calculated absolute orbital energies for different methods are shown in Table 1 and apply to both, the C₂ and the C_s conformer, because their values are equal to the second digit. The orbital geometries for the HOMO and LUMO of both T3DSH conformers calculated with the complete active space self-consistent field method are shown in Figure 1d.³⁹ The excited states are calculated using a time-dependent DFT (TDDFT) approach. Our results show that B3LYP/6-311+G** is sufficient to adequately model the T3DSH molecule. Higher basis sets like aug-TZvP and methods like CCSD yield very similar results while requiring significantly more calculation time. The absolute value of the HOMO energy is calculated following Koopmans theorem, taking the ionization energy of the molecule as the difference between the total energy of the ionized and the neutral molecule.⁴² The LUMO energy is calculated in a similar fashion from the molecule’s electron affinity. The calculated LUMO energy fits very well to the CV data, although a small discrepancy of 0.2 eV remains between theory and experiment for the HOMO. We stress that CV as well as quantum mechanical calculations of two pure, isolated components can only serve as a rough estimate for deriving the energy-level

diagram at the interface between the two constituents. Electronic interactions between PbS and T3DSH can lead to partial charge transfer, band bending, and other polarization effects, which potentially modify the diagram in Figure 1a.⁴³

Based on the calculated HOMO–LUMO gap of 3.4 eV, which is in agreement with the spectroscopic data in Figure 1c and considering the excitonic binding energy, it seems most likely that the CV reduction wave at -1.2 V vs Fc/Fc⁺ (Figure 1b, inset) does not directly correlate with a molecular frontier orbital of T3DSH, but has a different origin. In Figure 2, we

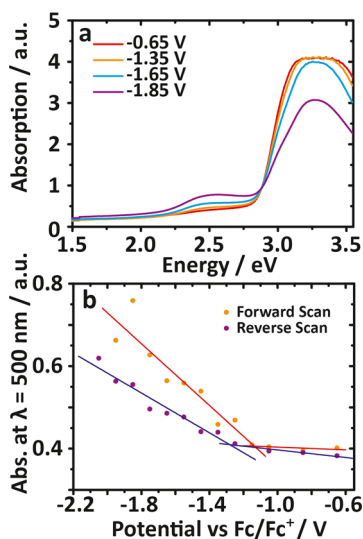


Figure 2. (a) Spectroelectrochemical measurement of T3DSH in acetone. The different colors indicate the potential applied during recording of the absorption spectrum. (b) Absorbance at $\lambda = 500$ nm of T3DSH as a function of the applied electrochemical potential.

use spectroelectrochemistry to elucidate the provenance of this unassigned reduction wave. An acetone solution of T3DSH and TBAHFP is filled into an optically transparent cell with a F:SnO₂ working electrode on glass, a silver wire reference electrode, and a platinum wire counter electrode. The cell is inserted into an optical spectrometer to measure the absorption spectrum while varying the potential to the working electrode. For increasingly reductive potentials, the molecule's HOMO–LUMO absorption band with a maximum at 3.3 eV diminishes, whereas a new band with a maximum at 2.5 eV emerges (Figure 2a). The emergence of this new absorption band is studied as a function of the applied reductive potential in Figure 2b. We observe a complete reversibility of its (dis-)appearance with a threshold potential of -1.2 V vs Fc/Fc⁺, suggesting that the reduction wave at the same potential in Figure 1b and the new absorption band are due to the same species.

To test the hypothesis that this new species may be due to the deprotonation of T3DSH, we added T3DSH to an acetone solution of NaOH. The absorption spectrum of this solution (Figure 1c, orange curve) exhibits a maximum at 2.48 eV and drastically diminished absorbance in the spectral window of the former HOMO–LUMO transition, in accordance with Figure 2a and our hypothesis. For further verification, we calculate the structure of T3DS²⁻ and find that the deprotonation of T3DSH changes the geometry into a fully planar C_{2v} symmetry (Figure 1d). Such planarization strengthens the aromatic character of the molecule, which

may shrink the HOMO–LUMO gap. Preliminary TDDFT calculations predict an S₀ → S₁ excitation energy of 2.68 eV, which supports this view. We conclude that the reduction wave at -1.2 V in Figure 1c is most likely due to negative charging of T3DSH. Incidentally, the same potential is required for charging the 1S_e state of PbS NCs as depicted in Figure 1a, which enables electronic coupling of the two semiconductors.

To explore such coupling, we prepare thin films of PbS/T3DSH at the liquid/air interface by exchanging the native oleic acid ligand sphere of PbS NCs partially with T3DSH based on an adapted technique first described by Dong et al.^{24,44} (see the Supporting Information for details). Vibrational spectroscopy verifies the successful incorporation of T3DSH into the ligand sphere, in that most characteristic T3DSH vibrations are retained in the ligand-exchanged film's spectrum (Figure 3). We note that the thiol band at 2500 cm⁻¹ is drastically reduced, indicating that a large portion of T3DSH resides on the PbS surface as the deprotonated anion.⁴⁵

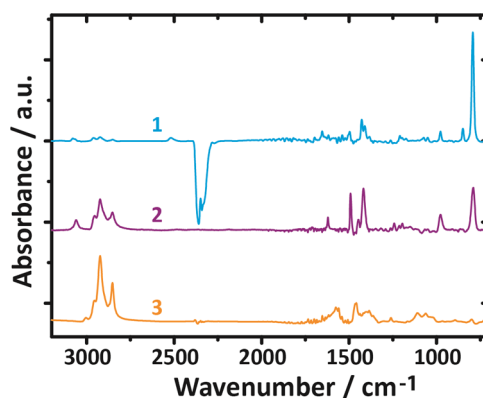


Figure 3. FTIR spectrum of (1) the pure T3DSH molecule, (2) PbS NCs functionalized with T3DSH, and (3) PbS NCs functionalized with oleic acid. Note: the band at 2300 cm⁻¹ is due to atmospheric CO₂.

We investigate the structure and morphology of the sample via scanning electron microscopy (SEM) and grazing incidence small-angle X-ray scattering (GISAXS) in Figure 4. In SEM, PbS/T3DSH films appear as highly ordered arrays of oriented NCs with extended domains, which are separated by frequent cracks. These cracks occur predominantly during transfer of the film from the liquid to a solid substrate and are found to be more frequent in multilayered films (about 150 nm thickness) than in mono- or bilayers. However, we observe that multilayers result in superior electronic properties, indicating that some of the cracks may be limited to the uppermost layers.

For a macroscopic investigation of the film's structure, we perform GISAXS, a technique that is widely used to determine structural details in similar particle films.^{46–50} The GISAXS pattern of a T3DSH-coupled NC film shown in Figure 4b can be indexed to an ordered superlattice with a body-centered cubic structure, a lattice constant of 8.4 nm, and a nearest-neighbor distance of 7.3 nm. Estimating the average NC diameter with 6.5 nm from the maximum of the first excitonic transition (1600 nm, see Figure S1) from established sizing curves allows us to gauge the interparticle spacing with 8 Å.^{51,52} This is significantly shorter than the initial interparticle spacing with oleic acid as the capping ligand (11–21 Å), but also much larger compared to ligand exchange with atomic passivation strategies (2–3 Å).^{6,24,53}

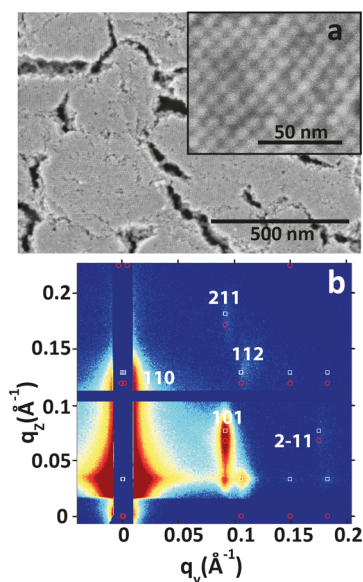


Figure 4. (a) SEM micrograph of a typical particle PbS/T3DSH film. The high-resolution inset shows the particle ordering in such assemblies. (b) GISAXS patterns of self-assembled PbS NCs after T3DSH ligand exchange, indexed according to a body-centered cubic structure.

To study the possible electronic coupling of PbS NCs by T3DSH, we perform electrochemically gated (EG) conductivity measurements. To this end, a T3DSH cross-linked PbS NC film is deposited onto a glass substrate with prepatterned, interdigitated Pt contacts separated by a gap of 5 μm to form a defined, conductive channel (Dropsens, G-IDEPT5). The two sides of the channel are connected to a bipotentiostat (CH Instruments, 760 E) to serve as the source and drain electrodes. The substrate is immersed into an electrolyte solution (acetone/TBAHFP) (0.1 M) together with a Pt counter electrode and a silver wire reference electrode. This setup allows measuring the steady-state conductance (G) across the NC film by keeping one side of the interdigitated channel (source) at a constant potential while cycling the other side of the channel (drain) around the fixed potential. Charging the NC film via varying the electrochemical potential across the electrolyte gives rise to an injected differential charge (measured by chronoamperometry, Figure S6), from which the accumulated charge (Q) is obtained by integration. In Figure 5a, we plot the potential dependent Q and G , which are related to the potential-dependent EG mobility (μ) plotted in Figure 5b through $\mu \sim \frac{d(G)}{d(Q)}$. The EG mobility exhibits a maximum for a gate potential of $-1.25(\pm 0.1)$ V vs Fc/Fc^+ ($-3.55(\pm 0.1)$ eV vs vacuum), which is in good agreement with the PbS $1S_c$ state. Our results are thus in accordance with the hypothesis of a PbS NC ensemble electronically coupled via their $1S_c$ states. We suggest that the molecular state involved in charging T3DSH identified in Figures 1 and 2 plays a pivotal role for this coupling.

The degree of electronic coupling is investigated by measuring the FET charge carrier mobility of PbS/T3DSH. Devices are prepared by depositing a thin film on top of a commercially available bottom-gate/bottom-contact FET substrate with prepatterned Au electrodes, 230 nm thermal oxide, and degenerately doped Si as gate contact. The FET mobilities are extracted from the transconductance measure-

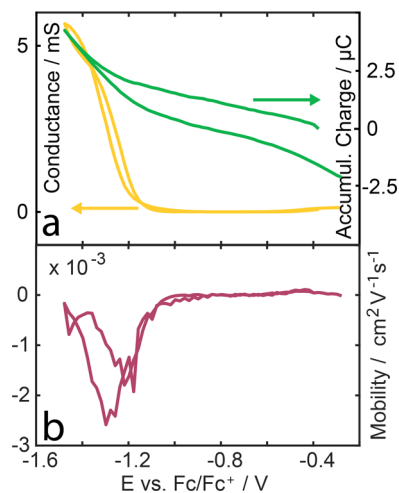


Figure 5. (a) Steady-state conductance (orange) and accumulated charge (green) vs the applied potential for a PbS/T3DSH film. (b) The extracted carrier mobility of the same sample as a function of the applied electrochemical potential.

ment at constant 5 V source–drain bias using the gradual channel approximation for the linear regime. Typical FET measurements, as presented in Figure 6, show electron

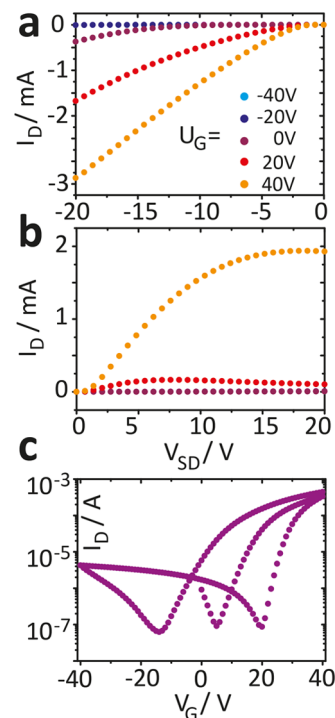


Figure 6. (a) Negative and (b) positive source–drain sweeps at the indicated gate voltage U_G for a typical PbS/T3DSH film. (c) Semilogarithmic transconductance of the same film.

mobilities of up to $0.2 \text{ cm}^2/(\text{V s})$. The slightly ambipolar material also shows hole transport with mobilities in the range of $10^{-3} \text{ cm}^2/(\text{V s})$. The calculated charge carrier concentration at a gate voltage of $V_g = 0$ V is on the order of $n(e) = 10^{13} \text{ cm}^{-3}$, whereas the on–off ratio is 10^4 . We tentatively attribute the hysteresis in the transconductance circles in Figure 6c to the charge trapping in the lowest layers of the PbS/T3DSH film and anticipate that reducing such injection barrier and/or

contact resistance is likely to further improve the FET mobilities.⁵⁴ We note that FET and EG mobilities can be quite different due to different measurement environments, geometries, and modes of charge carrier injection. Whereas EG measurements allow determining distinct transport channels, FET studies are most relevant for actual device applications.

The high electron mobility and low charge carrier concentration reported here are en par with state-of-the-art hybrid materials based on PbS NCs, which typically employ atomic passivation strategies and ultrashort interparticle spacings.^{14,18,55,56} Such transport properties are notoriously difficult to realize in PbS NCs due to the low formation enthalpy of electron trap states in lead chalcogenides, for instance, by adsorption of water/oxygen.^{54,57} They are pivotal parameters for the electron-transporting side in the PbS NC heterojunction solar cells or photodetectors.^{58,59} Significantly larger mobilities have only been realized for NC ensembles utilizing different NCs and/or upon necking/fusion into two-dimensional materials with a greatly altered electronic structure.^{60–63} An inherent drawback of NC ensembles with an ultrashort interparticle spacing is the trade-off between coupling and long-range order. Vanishingly small spacings invoke high mobilities but glass-like structure, whereas larger spacings maintain ample long-range order at the cost of reduced mobility.^{64–66} The material presented here combines both properties for the first time, enabling studies of the correlation between high mobility transport and long-range order in ensembles of spatially isolated NCs. Furthermore, the fundamental transport mechanism in NC ensembles coupled by the atomic passivation strategy has been discussed controversially, including some skepticism whether transport involves the NC 1S levels at all.^{60,67–69} The electrochemically gated transport measurements presented here are strong evidence that for the PbS–T3DSH system, the majority of charge carrier transport occurs indeed via the 1S_e level. We note that the observed hole mobility is similar to that measured in PbS NC ensembles capped with 1,2-ethanedithiol (EDT), a system with similar interparticle spacing, which is believed to operate by carrier tunneling through the ligand barrier.^{54,70} In contrast, the electron mobility in PbS–T3DSH is much larger than that for EDT-capping and cannot be explained with the reduced interparticle spacing. We hold the resonance illustrated in Figure 1a between the PbS 1S_e state and that of the charged T3DSH state responsible for this finding.

CONCLUSIONS

We demonstrate that cross-linking PbS NCs with semi-conducting 5,5''-dithiol-[2,2':5,2''-terthiophene] leads to a coupled organic–inorganic nanostructure with a large structural coherence and electron mobilities of 0.2 cm²/(V s). Electrochemically gated transport measurements indicate that electron transport occurs predominantly via the 1S_e state of the NC, supporting the view of coupled electronic states. This coupling is enabled by a near-resonant alignment of the NC 1S_e state with a suitable energy level in the negatively charged organic semiconductor. The combination of long-range order and ample electronic coupling in the same semiconductor nanocrystal array allows investigations of structure–transport correlations and the exploitation of potential transport anisotropies.

METHODS

PbS NCs and T3DSH were synthesized according to adapted literature procedures as detailed in the Supporting Information.^{36,66}

ASSOCIATED CONTENT

Supporting Information

The Supporting Information is available free of charge on the ACS Publications website at DOI: 10.1021/acsami.8b06044.

Detailed descriptions of experimental procedures, sample characterization, supporting figures, and description of electrochemical gating (PDF)

AUTHOR INFORMATION

Corresponding Author

*E-mail: marcus.scheele@uni-tuebingen.de

ORCID

Marcus Scheele: 0000-0002-2704-3591

Author Contributions

The manuscript was written through contributions of all authors. All authors have given approval to the final version of the manuscript.

Notes

The authors declare no competing financial interest.

ACKNOWLEDGMENTS

The authors acknowledge the DFG for support under Grants SCHE1905/3, SCHE1905/4, and SCHR700/25. Fruitful discussions with Bernd Speiser are gratefully acknowledged as well as Simon Schundelmeier for providing dried tetrahydrofurane. We also thank Elke Nadler, Institute of Physical and Theoretical Chemistry, University of Tübingen, for performing SEM/STEM measurements using a Hitachi SU 8030 SEM, which was partially funded by the DFG under contract INST 37/829-1 FUGG.

REFERENCES

- (1) Agranovich, V. M.; Gartstein, Y. N.; Litinskaya, M. Hybrid Resonant Organic-Inorganic Nanostructures for Optoelectronic Applications. *Chem. Rev.* **2011**, *111*, 5179–5214.
- (2) Reiss, P.; Couderc, E.; De Girolamo, J.; Pron, A. Conjugated Polymers/Semiconductor Nanocrystals Hybrid Materials-Preparation, Electrical Transport Properties and Applications. *Nanoscale* **2011**, *3*, 446–489.
- (3) Scheele, M.; Bruetting, W.; Schreiber, F. Coupled Organic-Inorganic Nanostructures. *Phys. Chem. Chem. Phys.* **2015**, *17*, 97–111.
- (4) Voznyy, O.; Sutherland, B. R.; Ip, A. H.; Zhitomirsky, D.; Sargent, E. H. Engineering Charge Transport by Heterostructuring Solution-Processed Semiconductors. *Nat. Rev. Mater.* **2017**, *2*, No. 17026.
- (5) Hong, J.; Hou, B.; Lim, J.; Pak, S.; Kim, B.-S.; Cho, Y.; Lee, J.; Lee, Y.-W.; Giraud, P.; Lee, S.; Park, J. B.; Morris, S. M.; Snaith, H. J.; Sohn, J. I.; Cha, S.; Kim, J. M. Enhanced Charge Carrier Transport Properties in Colloidal Quantum Dot Solar Cells via Organic and Inorganic Hybrid Surface Passivation. *J. Mater. Chem. A* **2016**, *4*, 18769–18775.
- (6) Ip, A. H.; Thon, S. M.; Hoogland, S.; Voznyy, O.; Zhitomirsky, D.; Debnath, R.; Levina, L.; Rollny, L. R.; Carey, G. H.; Fischer, A.; Kemp, K. W.; Kramer, I. J.; Ning, Z.; Labelle, A. J.; Chou, K. W.; Amassian, A.; Sargent, E. H. Hybrid Passivated Colloidal Quantum Dot Solids. *Nat. Nanotechnol.* **2012**, *7*, 577–582.
- (7) Jin, S.; Tagliazucchi, M.; Son, H.-J.; Harris, R. D.; Aruda, K. O.; Weinberg, D. J.; Nepomnyashchii, A. B.; Farha, O. K.; Hupp, J. T.; Weiss, E. A. Enhancement of the Yield of Photoinduced Charge Separation in Zinc Porphyrin-Quantum Dot Complexes by a

Bis(dithiocarbamate) Linkage. *J. Phys. Chem. C* **2015**, *119*, 5195–5202.

(8) Lauth, J.; Grimaldi, G.; Kinge, S.; Houtepen, A. J.; Siebbeles, L. D. A.; Scheele, M. Ultrafast Charge Transfer and Upconversion in Zinc β -Tetraaminophthalocyanine-Functionalized PbS Nanostructures Probed by Transient Absorption Spectroscopy. *Angew. Chem.* **2017**, *129*, 14249–14253.

(9) Mongin, C.; Garakyaraghi, S.; Razgoniaeva, N.; Zamkov, M.; Castellano, F. N. Direct Observation of Triplet Energy Transfer from Semiconductor Nanocrystals. *Science* **2016**, *351*, 369–372.

(10) Adinolfi, V.; Sargent, E. H. Photovoltage Field-Effect Transistors. *Nature* **2017**, *542*, 324–327.

(11) Lan, X.; Voznyy, O.; de Arquer, F. P. G.; Liu, M.; Xu, J.; Proppe, A. H.; Walters, G.; Fan, F.; Tan, H.; Liu, M.; Yang, Z.; Hoogland, S.; Sargent, E. H. 10.6% Certified Colloidal Quantum Dot Solar Cells via Solvent-Polarity-Engineered Halide Passivation. *Nano Lett.* **2016**, *16*, 4630–4634.

(12) Talapin, D. V.; Murray, C. B. PbSe Nanocrystal Solids for n- and p-Channel Thin Film Field-Effect Transistors. *Science* **2005**, *310*, 86–89.

(13) Yu, D.; Wang, C.; Guyot-Sionnest, P. n-Type Conducting CdSe Nanocrystal Solids. *Science* **2003**, *300*, 1277–1280.

(14) Balazs, D. M.; Dirin, D. N.; Fang, H.-H.; Protesescu, L.; ten Brink, G. H.; Kooi, B. J.; Kovalenko, M. V.; Loi, M. A. Counterion-Mediated Ligand Exchange for PbS Colloidal Quantum Dot Superlattices. *ACS Nano* **2015**, *9*, 11951–11959.

(15) Bisri, S. Z.; Piliago, C.; Yarema, M.; Heiss, W.; Loi, M. A. Low Driving Voltage and High Mobility Ambipolar Field-Effect Transistors with PbS Colloidal Nanocrystals. *Adv. Mater.* **2013**, *25*, 4309–4314.

(16) Fafarman, A. T.; Koh, W.; Diroll, B. T.; Kim, D. K.; Ko, D.-K.; Oh, S. J.; Ye, X.; Doan-Nguyen, V.; Crump, M. R.; Reifsnnyder, D. C.; Murray, C. B.; Kagan, C. R. Thiocyanate-Capped Nanocrystal Colloids: Vibrational Reporter of Surface Chemistry and Solution-Based Route to Enhanced Coupling in Nanocrystal Solids. *J. Am. Chem. Soc.* **2011**, *133*, 15753–15761.

(17) Liu, Y.; Tolentino, J.; Gibbs, M.; Ihly, R.; Perkins, C. L.; Liu, Y.; Crawford, N.; Hemminger, J. C.; Law, M. PbSe Quantum Dot Field-Effect Transistors with Air-Stable Electron Mobilities above $7 \text{ cm}^2 \text{V}^{-1} \text{s}^{-1}$. *Nano Lett.* **2013**, *13*, 1578–1587.

(18) Oh, S. J.; Berry, N. E.; Choi, J.-H.; Gauling, E. A.; Lin, H.; Paik, T.; Diroll, B. T.; Muramoto, S.; Murray, C. B.; Kagan, C. R. Designing High-Performance PbS and PbSe Nanocrystal Electronic Devices through Stepwise, Post-Synthesis, Colloidal Atomic Layer Deposition. *Nano Lett.* **2014**, *14*, 1559–1566.

(19) Oh, S. J.; Berry, N. E.; Choi, J.-H.; Gauling, E. A.; Paik, T.; Hong, S.-H.; Murray, C. B.; Kagan, C. R. Stoichiometric Control of Lead Chalcogenide Nanocrystal Solids to Enhance Their Electronic and Optoelectronic Device Performance. *ACS Nano* **2013**, *7*, 2413–2421.

(20) Vörös, M.; Brawand, N. P.; Galli, G. Hydrogen Treatment as a Detergent of Electronic Trap States in Lead Chalcogenide Nanoparticles. *Chem. Mater.* **2017**, *29*, 2485–2493.

(21) André, A.; Zherebetskyy, D.; Hanifi, D.; He, B.; Samadi Khoshkhoo, M.; Jankowski, M.; Chasse, T.; Wang, L.-W.; Schreiber, F.; Salleo, A.; Liu, Y.; Scheele, M. Toward Conductive Mesocrystalline Assemblies: PbS Nanocrystals Cross-Linked with Tetrathiafulvalene Dicarboxylate. *Chem. Mater.* **2015**, *27*, 8105–8115.

(22) Scheele, M.; Hanifi, D.; Zherebetskyy, D.; Chourou, S. T.; Axnanda, S.; Rancatore, B. J.; Thorkelsson, K.; Xu, T.; Liu, Z.; Wang, L.-W.; Liu, Y.; Alivisatos, A. P. PbS Nanoparticles Capped with Tetrathiafulvalene-tetracarboxylate: Utilizing Energy Level Alignment for Efficient Carrier Transport. *ACS Nano* **2014**, *8*, 2532–2540.

(23) Frederick, M. T.; Amin, V. A.; Swenson, N. K.; Ho, A. Y.; Weiss, E. A. Control of Exciton Confinement in Quantum Dot-Organic Complexes through Energetic Alignment of Interfacial Orbitals. *Nano Lett.* **2013**, *13*, 287–292.

(24) Maiti, S.; André, A.; Banerjee, R.; Hagenlocher, J.; Konovalov, O.; Schreiber, F.; Scheele, M. Monitoring Self-Assembly and Ligand

Exchange of PbS Nanocrystal Superlattices at the Liquid/Air Interface in Real Time. *J. Phys. Chem. Lett.* **2018**, *9*, 739–744.

(25) Zaluzhnyy, I. A.; Kurta, R. P.; André, A.; Gorobtsov, O. Y.; Rose, M.; Skopintsev, P.; Besedin, I.; Zozulya, A. V.; Sprung, M.; Schreiber, F.; Vartanyants, I. A.; Scheele, M. Quantifying Angular Correlations between the Atomic Lattice and the Superlattice of Nanocrystals Assembled with Directional Linking. *Nano Lett.* **2017**, *17*, 3511–3517.

(26) Axnanda, S.; Scheele, M.; Crumlin, E.; Mao, B.; Chang, R.; Rani, S.; Faiz, M.; Wang, S.; Alivisatos, A. P.; Liu, Z. Direct Work Function Measurement by Gas Phase Photoelectron Spectroscopy and Its Application on PbS Nanoparticles. *Nano Lett.* **2013**, *13*, 6176–6182.

(27) Brown, P. R.; Kim, D.; Lunt, R. R.; Zhao, N.; Bawendi, M. G.; Grossman, J. C.; Bulović, V. Energy Level Modification in Lead Sulfide Quantum Dot Thin Films through Ligand Exchange. *ACS Nano* **2014**, *8*, 5863–5872.

(28) Jasieniak, J.; Califano, M.; Watkins, S. E. Size-Dependent Valence and Conduction Band-Edge Energies of Semiconductor Nanocrystals. *ACS Nano* **2011**, *5*, 5888–5902.

(29) Beek, W. J. E.; Janssen, R. A. J. Photoinduced Electron Transfer in Heterosupramolecular Assemblies of TiO₂ Nanoparticles and Terthiophene Carboxylic Acid in Apolar Solvents. *Adv. Funct. Mater.* **2002**, *12*, 519–525.

(30) Heinemann, M. D.; Maydell, K. von; Zutz, F.; Kolny-Olesiak, J.; Borchert, H.; Riedel, I.; Parisi, J. Photo-induced Charge Transfer and Relaxation of Persistent Charge Carriers in Polymer/Nanocrystal Composites for Applications in Hybrid Solar Cells. *Adv. Funct. Mater.* **2009**, *19*, 3788–3795.

(31) Milliron, D. J.; Alivisatos, A. P.; Pitois, C.; Edder, C.; Fréchet, J. M. J. Electroactive Surfactant Designed to Mediate Electron Transfer Between CdSe Nanocrystals and Organic Semiconductors. *Adv. Mater.* **2003**, *15*, 58–61.

(32) Radychev, N.; Lokteva, I.; Witt, F.; Kolny-Olesiak, J.; Borchert, H.; Parisi, J. Physical Origin of the Impact of Different Nanocrystal Surface Modifications on the Performance of CdSe/P3HT Hybrid Solar Cells. *J. Phys. Chem. C* **2011**, *115*, 14111–14122.

(33) Radychev, N.; Scheunemann, D.; Kruszynska, M.; Frevert, K.; Miranti, R.; Kolny-Olesiak, J.; Borchert, H.; Parisi, J. Investigation of the Morphology and Electrical Characteristics of Hybrid Blends Based on Poly(3-hexylthiophene) and Colloidal CuInS₂ Nanocrystals of Different Shapes. *Org. Electron.* **2012**, *13*, 3154–3164.

(34) Witt, E.; Witt, F.; Trautwein, N.; Fenske, D.; Neumann, J.; Borchert, H.; Parisi, J.; Kolny-Olesiak, J. Synthesis of Lead Chalcogenide Nanocrystals and Study of Charge Transfer in Blends of PbSe Nanocrystals and Poly(3-hexylthiophene). *Phys. Chem. Chem. Phys.* **2012**, *14*, 11706–11714.

(35) Pommerehne, J.; Vestweber, H.; Guss, W.; Mahrt, R. F.; Bässler, H.; Porsch, M.; Daub, J. Efficient Two Layer LEDs on a Polymer Blend Basis. *Adv. Mater.* **1995**, *7*, 551–554.

(36) de Boer, B.; Meng, H.; Perepichka, D. F.; Zheng, J.; Frank, M. M.; Chabal, Y. J.; Bao, Z. Synthesis and Characterization of Conjugated Mono- and Dithiol Oligomers and Characterization of Their Self-Assembled Monolayers. *Langmuir* **2003**, *19*, 4272–4284.

(37) Berlin, A.; Zotti, G.; Schiavon, G.; Zecchin, S. Adsorption of Carboxyl-Terminated Dithiophene and Terthiophene Molecules on ITO Electrodes and Their Electrochemical Coupling to Polymer Layers. The Influence of Molecular Geometry. *J. Am. Chem. Soc.* **1998**, *120*, 13453–13460.

(38) Zotti, G.; Zecchin, S.; Vercelli, B.; Berlin, A.; Grimoldi, S.; Groenendaal, L.; Bertoncello, R.; Natali, M. Surface-Initiated Polymerization of Thiophene and Pyrrole Monomers on Poly(terthiophene) Films and Oligothiophene Monolayers. *Chem. Mater.* **2005**, *17*, 3681–3694.

(39) Kölle, P.; Schnappinger, T.; de Vivie-Riedle, R. Deactivation Pathways of Thiophene and Oligothiophenes: Internal Conversion versus Intersystem Crossing. *Phys. Chem. Chem. Phys.* **2016**, *18*, 7903–7915.

- (40) Caricato, M. Absorption and Emission Spectra of Solvated Molecules with the EOM-CCSD-PCM Method. *J. Chem. Theory Comput.* **2012**, *8*, 4494–4502.
- (41) Miertuš, S.; Scrocco, E.; Tomasi, J. Electrostatic Interaction of a Solute with a Continuum. A Direct Utilization of Ab Initio Molecular Potentials for the Prevision of Solvent Effects. *Chem. Phys.* **1981**, *55*, 117–129.
- (42) Koopmans, T. Über die Zuordnung von Wellenfunktionen und Eigenwerten zu den Einzelnen Elektronen Eines Atoms. *Physica* **1934**, *1*, 104–113.
- (43) Samadi Khoshkhoo, M.; Peisert, H.; Chassé, T.; Scheele, M. The Role of the Density of Interface States in Interfacial Energy Level Alignment of PTCDA. *Org. Electron.* **2017**, *49*, 249–254.
- (44) Dong, A.; Chen, J.; Oh, S. J.; Koh, W.; Xiu, F.; Ye, X.; Ko, D.-K.; Wang, K. L.; Kagan, C. R.; Murray, C. B. Multiscale Periodic Assembly of Striped Nanocrystal Superlattice Films on a Liquid Surface. *Nano Lett.* **2011**, *11*, 841–846.
- (45) Tour, J. M.; Jones, L.; Pearson, D. L.; Lamba, J. J. S.; Burgin, T. P.; Whitesides, G. M.; Allara, D. L.; Parikh, A. N.; Atre, S. Self-Assembled Monolayers and Multilayers of Conjugated Thiols, α,ω -Dithiols, and Thioacetyl-Containing Adsorbates. Understanding Attachments between Potential Molecular Wires and Gold Surfaces. *J. Am. Chem. Soc.* **1995**, *117*, 9529–9534.
- (46) Geuchies, J. J.; van Overbeek, C.; Evers, W. H.; Goris, B.; de Backer, A.; Gantapara, A. P.; Rabouw, F. T.; Hilhorst, J.; Peters, J. L.; Kononov, O.; Petukhov, A. V.; Dijkstra, M.; Siebbeles, L. D. A.; van Aert, S.; Bals, S.; Vanmaekelbergh, D. In Situ Study of the Formation Mechanism of Two-Dimensional Superlattices from PbSe Nanocrystals. *Nat. Mater.* **2016**, *15*, 1248–1254.
- (47) Maiti, S.; Sanyal, M. K.; Jana, M. K.; Runge, B.; Murphy, B. M.; Biswas, K.; Rao, C. N. R. Evidence of Contact Epitaxy in the Self-Assembly of HgSe Nanocrystals Formed at a Liquid-Liquid Interface. *J. Phys.: Condens. Matter* **2017**, *29*, No. 095101.
- (48) Novák, J.; Banerjee, R.; Kornowski, A.; Jankowski, M.; Andre, A.; Weller, H.; Schreiber, F.; Scheele, M. Site-Specific Ligand Interactions Favor the Tetragonal Distortion of PbS Nanocrystal Superlattices. *ACS Appl. Mater. Interfaces* **2016**, *8*, 22526–22533.
- (49) van der Stam, W.; Rabouw, F. T.; Vonk, S. J. W.; Geuchies, J. J.; Lighthart, H.; Petukhov, A. V.; de Mello Donega, C. Oleic Acid-Induced Atomic Alignment of ZnS Polyhedral Nanocrystals. *Nano Lett.* **2016**, *16*, 2608–2614.
- (50) Weidman, M. C.; Smilgies, D.-M.; Tisdale, W. A. Kinetics of the Self-Assembly of Nanocrystal Superlattices Measured by Real-Time In Situ X-ray Scattering. *Nat. Mater.* **2016**, *15*, 775–781.
- (51) Moreels, I.; Lambert, K.; Smeets, D.; De Muynck, D.; Nollet, T.; Martins, J. C.; Vanhaecke, F.; Vantomme, A.; Delerue, C.; Allan, G.; Hens, Z. Size-Dependent Optical Properties of Colloidal PbS Quantum Dots. *ACS Nano* **2009**, *3*, 3023–3030.
- (52) Segets, D.; Lucas, J. M.; Klupp Taylor, R. N.; Scheele, M.; Zheng, H.; Alivisatos, A. P.; Peukert, W. Determination of the Quantum Dot Band Gap Dependence on Particle Size from Optical Absorbance and Transmission Electron Microscopy Measurements. *ACS Nano* **2012**, *6*, 9021–9032.
- (53) Wang, Z.; Schliehe, C.; Bian, K.; Dale, D.; Bassett, W. A.; Hanrath, T.; Klinke, C.; Weller, H. Correlating Superlattice Polymorphs to Internanoparticle Distance, Packing Density, and Surface Lattice in Assemblies of PbS Nanoparticles. *Nano Lett.* **2013**, *13*, 1303–1311.
- (54) Balazs, D. M.; Nugraha, M. I.; Bisri, S. Z.; Sytnyk, M.; Heiss, W.; Loi, M. A. Reducing Charge Trapping in PbS Colloidal Quantum Dot Solids. *Appl. Phys. Lett.* **2014**, *104*, No. 112104.
- (55) Oh, S. J.; Straus, D. B.; Zhao, T.; Choi, J.-H.; Lee, S.-W.; Gauldin, E. A.; Murray, C. B.; Kagan, C. R. Engineering the Surface Chemistry of Lead Chalcogenide Nanocrystal Solids to Enhance Carrier Mobility and Lifetime in Optoelectronic Devices. *Chem. Commun.* **2017**, *53*, 728–731.
- (56) Zhitomirsky, D.; Furukawa, M.; Tang, J.; Stadler, P.; Hoogland, S.; Voznyy, O.; Liu, H.; Sargent, E. H. N-Type Colloidal-Quantum-Dot Solids for Photovoltaics. *Adv. Mater.* **2012**, *24*, 6181–6185.
- (57) Leschkies, K. S.; Kang, M. S.; Aydil, E. S.; Norris, D. J. Influence of Atmospheric Gases on the Electrical Properties of PbSe Quantum-Dot Films. *J. Phys. Chem. C* **2010**, *114*, 9988–9996.
- (58) de Arquer, F. P. G.; Armin, A.; Meredith, P.; Sargent, E. H. Solution-Processed Semiconductors for Next-Generation Photodetectors. *Nat. Rev. Mater.* **2017**, *2*, No. 16100.
- (59) Zhitomirsky, D.; Voznyy, O.; Levina, L.; Hoogland, S.; Kemp, K. W.; Ip, A. H.; Thon, S. M.; Sargent, E. H. Engineering Colloidal Quantum Dot Solids within and beyond the Mobility-Invariant Regime. *Nat. Commun.* **2014**, *5*, No. 3803.
- (60) Choi, J.-H.; Fafarman, A. T.; Oh, S. J.; Ko, D.-K.; Kim, D. K.; Diroll, B. T.; Muramoto, S.; Gillen, J. G.; Murray, C. B.; Kagan, C. R. Bandlike Transport in Strongly Coupled and Doped Quantum Dot Solids: A Route to High-Performance Thin-Film Electronics. *Nano Lett.* **2012**, *12*, 2631–2638.
- (61) Chung, D. S.; Lee, J.-S.; Huang, J.; Nag, A.; Ithurria, S.; Talapin, D. V. Low Voltage, Hysteresis Free, and High Mobility Transistors from All-Inorganic Colloidal Nanocrystals. *Nano Lett.* **2012**, *12*, 1813–1820.
- (62) Evers, W. H.; Schins, J. M.; Aerts, M.; Kulkarni, A.; Capiod, P.; Berthe, M.; Grandidier, B.; Delerue, C.; van der Zant, H. S. J.; van Overbeek, C.; Peters, J. L.; Vanmaekelbergh, D.; Siebbeles, L. D. A. High Charge Mobility in Two-Dimensional Percolative Networks of PbSe Quantum Dots Connected by Atomic Bonds. *Nat. Commun.* **2015**, *6*, No. 8195.
- (63) Lee, J.-S.; Kovalenko, M. V.; Huang, J.; Chung, D. S.; Talapin, D. V. Band-Like Transport, High Electron Mobility and High Photoconductivity in All-Inorganic Nanocrystal Arrays. *Nat. Nanotechnol.* **2011**, *6*, 348–352.
- (64) Dong, A.; Jiao, Y.; Milliron, D. J. Electronically Coupled Nanocrystal Superlattice Films by In Situ Ligand Exchange at the Liquid-Air Interface. *ACS Nano* **2013**, *7*, 10978–10984.
- (65) Liu, Y.; Gibbs, M.; Puthussery, J.; Gaik, S.; Ihly, R.; Hillhouse, H. W.; Law, M. Dependence of Carrier Mobility on Nanocrystal Size and Ligand Length in PbSe Nanocrystal Solids. *Nano Lett.* **2010**, *10*, 1960–1969.
- (66) Weidman, M. C.; Yager, K. G.; Tisdale, W. A. Interparticle Spacing and Structural Ordering in Superlattice PbS Nanocrystal Solids Undergoing Ligand Exchange. *Chem. Mater.* **2015**, *27*, 474–482.
- (67) Jang, J.; Liu, W.; Son, J. S.; Talapin, D. V. Temperature-Dependent Hall and Field-Effect Mobility in Strongly Coupled All-Inorganic Nanocrystal Arrays. *Nano Lett.* **2014**, *14*, 653–662.
- (68) Norman, Z. M.; Anderson, N. C.; Owen, J. S. Electrical Transport and Grain Growth in Solution-Cast, Chloride-Terminated Cadmium Selenide Nanocrystal Thin Films. *ACS Nano* **2014**, *8*, 7513–7521.
- (69) Scheele, M. To Be or not to Be: Band-Like Transport in Quantum Dot Solids. *Z. Phys. Chem.* **2015**, *229*, 167–178.
- (70) Osedach, T. P.; Zhao, N.; Andrew, T. L.; Brown, P. R.; Wanger, D. D.; Strasfeld, D. B.; Chang, L.-Y.; Bawendi, M. G.; Bulović, V. Bias-Stress Effect in 1,2-Ethanedithiol-Treated PbS Quantum Dot Field-Effect Transistors. *ACS Nano* **2012**, *6*, 3121–3127.